minerals

MDPI

Article

Characterisation of the Grain Morphology of Artificial Minerals (EnAMs) in Lithium Slags by Correlating Multi-Dimensional 2D and 3D Methods

Cindytami Rachmawati [1,*], Joao Weiss [2,*], Hugo Ignacio Lucas [2], Erik Löwer [1], Thomas Leißner [1], Doreen Ebert [3], Robert Möckel [3], Bernd Friedrich [2] and Urs Alexander Peuker [1]

1 Institute of Mechanical Process Engineering and Mineral Processing, Technische Universität Bergakademie Freiberg, 09599 Freiberg, Germany; erik.loewer@mvtat.tu-freiberg.de (E.L.); thomas.leissner@mvtat.tu-freiberg.de (T.L.); urs.peuker@mvtat.tu-freiberg.de (U.A.P.)
2 Institute of Process Metallugy and Metal Recycling, RWTH Aachen University, 52056 Aachen, Germany; hlucas@metallurgie.rwth-aachen.de (H.I.L.); bfriedrich@ime-aachen.de (B.F.)
3 Helmholtz-Zentrum Dresden-Rossendorf, Helmholtz Institute Freiberg for Resource Technology, Chemnitzer Straße 40, 09599 Freiberg, Germany; d.ebert@hzdr.de (D.E.); r.moeckel@hzdr.de (R.M.)
* Correspondence: cindytami.rachmawati@mvtat.tu-freiberg.de (C.R.); jweiss@metallurgie.rwth-aachen.de (J.W.)

Abstract: Slags from the metallurgical recycling process are an important source of resources classified as critical elements by the EU. One example is lithium from Li-ion battery recycling. In this context, the thermodynamic properties of the recycled component system play a significant role in the formation of the Li-bearing phases in the slag, in this case, $LiAlO_2$. $LiAlO_2$ crystal formation could be engineered and result in varying sizes and occurrences by different metallurgical processing conditions. This study uses pure ingredients to provide a synthetic model material which can be used to generate the valuable phase in the slag, or so-called engineered artificial minerals (EnAMs). The aim is to investigate the crystallisation of $LiAlO_2$ as an EnAM by controlling the cooling conditions of the model slag to optimise the EnAM formed during crystallisation. Characterisation of the EnAMs is an important step before further mechanically processing the material to recover the valuable element Li, the Li-bearing species, respectively. Investigations are conducted using powder X-ray diffraction (XRD), X-ray fluorescence (µXRF), and X-ray Computer Tomography (XCT) on two different artificial lithium slags from MnO-Al_2O_3-SiO_2-CaO systems with different cooling temperature gradients. The result shows the different EnAM morphology along the height of the slag, which is formed under different slag production conditions in a semi-pilot scale experiment of 5 kg. Based on the different EnAM morphologies, three defined qualities of the EnAM are identified: granular, dendritic, and irregular-shape EnAM.

Keywords: engineered artificial mineral (EnAM); slag characterisation; $LiAlO_2$ (lithium aluminate); X-ray micro-CT; micro-XRF

check for updates

Citation: Rachmawati, C.; Weiss, J.; Lucas, H.I.; Löwer, E.; Leißner, T.; Ebert, D.; Möckel, R.; Friedrich, B.; Peuker, U.A. Characterisation of the Grain Morphology of Artificial Minerals (EnAMs) in Lithium Slags by Correlating Multi-Dimensional 2D and 3D Methods. *Minerals* **2024**, *14*, 130. https://doi.org/10.3390/min14020130

Academic Editor: Rafael Santos

Received: 15 December 2023
Revised: 17 January 2024
Accepted: 23 January 2024
Published: 25 January 2024

Copyright: © 2024 by the authors. Licensee MDPI, Basel, Switzerland. This article is an open access article distributed under the terms and conditions of the Creative Commons Attribution (CC BY) license (https://creativecommons.org/licenses/by/4.0/).

1. Introduction

The increase in the demand for electric automobiles as one of the initiatives for reducing climate change has also increased lithium-ion battery (LIB) consumption [1]. The World Economic Forum reported that 2 billion electric vehicles are required by 2050 to reduce emissions to be able to balance the global greenhouse gas emissions from human activities [2]. An LIB pack for a single vehicle contains around 8 kg of lithium [3]. McKinsey [4] has forecasted that the market growth of LIB until 2030 could reach 30% annually. The question would be whether there are enough lithium supplies to produce Li-ion batteries, especially when the demand surges every year and the lithium resource scarcity increases [2]. To overcome this problem, several studies on Li-ion battery recycling have been carried out to try to recover lithium [5–10].

For pyrometallurgical recycling, two processes, referred to as direct and multi-step smelting, are outlined and economically analysed for the recycling of Li-ion batteries. In the direct smelting approach, batteries are disassembled and subjected to a shaft furnace with distinct temperature zones, including a preheating stage, a pyrolysis zone for volatilization, and a final smelting reduction phase. The multi-step method involves additional mechanical pre-treatments, including pyrolysis and sieving, resulting in a fine fraction that requires pelletization before entering the electric arc furnace step, ultimately leading to comparable product phases with variations in mass balances and metal distribution. From these processes, various products and byproducts are generated, including a metal alloy, exhaust gas and flue dust, and slag [11,12].

Slag from the pyrometallurgical recycling of LIBs is a source of critical elements [13,14]. The pyrometallurgy process uses heat energy to melt and separate the metals (such as cobalt, nickel, copper, and iron) from the pre-processed/pre-treated LIBs [13,15–17]. The rest of the materials will be considered by-products/waste, oxidized, and separated and finally solidified as slag. Lithium, as a light and non-noble element, also goes to slag and forms phases that are associated with Al and Si [18]. This slag is usually used as an additive for cement in construction [19]. The remaining valuable element, which, in this case, is Li, is thus lost in any material cycle, since it is immobilized within the slag structure. Lithium aluminate ($LiAlO_2$) is one of the phases potentially formed from the reaction between Li and Al in the lithium battery slag [20,21], which requires further attention as Li should be kept in the battery material cycle. Prior studies on slags without manganese (Mn) demonstrated effective Li-enrichment through chemical optimisation; the presence of Mn complicates recovery due to dispersion among oxides and silicates, which are known to be particularly unsuitable for flotation [8]. Therefore, the slag has to be treated, so that, with further mechanical processing, it becomes possible to extract the lithium via extracting the lithium aluminate.

During the solidification of the slag, the crystal formation depends on the metallurgical processing conditions, such as chemical composition [22] and cooling conditions [23]. Rapid cooling will result in a higher content of an amorphous component because the solidification process occurs without the development of a crystalline structure [24]. Controlled cooling conditions can lead to a defined phase transformation and consequently allow for a better understanding of how the slag formation should be manipulated for more-effective subsequent mechanical processing.

Crystal formation plays a central role in optimising the recovery of the critical elements due to the EnAM concept. Given that the degree of liberation is size-dependent, it is possible to liberate crystals after crushing and milling them at a larger size, when the initial crystal size is larger as well. This will enhance the efficiency of the mechanical slag processing since less energy is required for comminution. The next step is the physical separation, where both the grade and the recovery depend on the degree of liberation achieved in the upstream process steps [25,26]. Further downstream liberation also affects the hydrometallurgical extraction of lithium, which uses flotation as a pre-concentration step and is one of the prevalent methods for lithium extraction [15].

Some research has been carried out into artificial lithium slag systems, focusing on the phase composition and speciation [20,21,27,28]. Pure ingredients are used in the artificial slag to provide a synthetic model material with the valuable phase formation in the slag, EnAM, respectively. The phase of interest or the EnAM is $LiAlO_2$, as the recoverable [29] and stable lithium phase within the lithium slag [8]. Another study on EnAM generation in a copper-containing WEEE slag with different cooling rates relative to its position has also been carried out to investigate the phase formation, internal structure, and its recyclability [23]. Depending on further processing, different grain morphology may generate different results. Variation in grain sizes and shapes across the slag body may lead to different breakage and, therefore, liberation mechanisms [30,31]. Adjusting the slag-forming parameters is an important factor in optimising the EnAM formation, and resulting in a higher potential to optimise the recovery of lithium from the slag [32].

In this study, a technical scale experiment for producing artificial lithium slag is tailored with the aim of forming optimised Li-EnAM grains. The different types of crystals formed in the synthetic lithium slags with different cooling conditions used for solidification are studied. By using the characterisation method in this study, one can analyse the grain morphology throughout the whole sample to understand the slag structure and the crystal formation within the whole slag body produced in 3D. The outcome of this study is important as an evaluation prior to the mechanical processing phase. The results will be applied to optimise the lithium slag processing conditions by investigating the crystals formed under different process conditions. The main objective of this study is to analyse the valuable lithium phases formed in relation to their production parameters to find the optimum condition for further processing steps.

2. Materials and Methods

2.1. Sample Material

2.1.1. Slag Production

The artificial slag composition developed in this study was based on the chemical compositions in the work by Elwert et al. [21] shown in Table 1. The artificial slag feed composition consists of, Li_2O, MnO, Al_2O_3, SiO_2, and CaO. For the experiments, lithium was used in its carbonate form (99.99%, Alfa Aesar, Karlsruhe, Germany) instead of lithium oxide, because of availability issues. Li_2CO_3 decomposes to Li_2O during the heating process, due to the CO_2 release, so for further explanations and calculations, Li_2O was regarded. Manganese oxide and Alumina, α-phase, from Alfa Aesar with a purity of >99.99% were used. Burnt lime from Carl Roth (Karlsruhe, Germany) with a CaO content of $\geq$96% was used. Quartz was sourced from Heraeus Quarzglas GmbH & Co. (Hanau, Germany). For the calculations and experiments, a content of 100 wt.% for all materials was assumed. The detailed composition of the artificial slag used in this study can be seen in Table 2 below. Both Slag A and B were produced using the same feed composition. The SiO_2, CaO, and Al_2O_3 contents for the artificial slag were chosen to achieve a melting point below 1500 °C with a good compromise on viscosity.

Table 1. Composition of high-manganese-content lithium-containing slag investigated by Elwert et. al. [21].

Slag System	Li_2O	MnO_2	MgO	Al_2O_3	SiO_2	CaO
High Manganese Content	8.3%	9.5%	1.4%	44.5%	17.5%	16.1%

Table 2. The feed composition and cooling rate of the artificial slag.

Sample Name	Li_2O	MnO	Al_2O_3	SiO_2	CaO	Cooling Rate
Slag A	8.5%	10.4%	45.3%	18.9%	16.9%	50 °C/h
Slag B						25 °C/h

The experiments were carried out in an electric furnace (Thermo-Star, Aachen, Germany) heated by SiC rods, with an internal volume of 35 L and power of 46 kW, under an air atmosphere (Figure 1). For the experiments, clay–graphite crucibles type A20 from Atlantic Schmelztiegel Christoph Goebel GmbH (Grossalmerode, Germany) were filled with the slag feed. The crucible has a bottom diameter (d), upper diameter (D), and height (h) of 140 mm, 200 mm, and 255 mm, respectively. The crucible has a wall thickness of around 30 mm. The compounds were heated up to 1500 °C and, successively, the molten slag was kept at this temperature for 5 h for homogenization. After the holding time, the controlled cooling procedure was started as the slag was firstly cooled down to 1050 °C and then kept at this temperature for another 6 h. This holding time serves to create a

better solidification process and homogenization of the slag and increases the grain size regarding the $LiAlO_2$ phases. Subsequently, the slag was again controlled and cooled down to room temperature. During the experiments, the slag temperature was monitored with a precision thermocouple (Type C), following either the 50 or 25 °C/h cooling rates specified in Table 1, ensuring a controlled phase transformation in order to perform a thorough 3D characterisation. Here, two cooling rates have been studied, 50 and 25 °C/h (Table 2). Higher cooling rates resulted in a material with an elevated amorphous content, so these cooling rates were chosen to evaluate the 3D characterisation techniques.

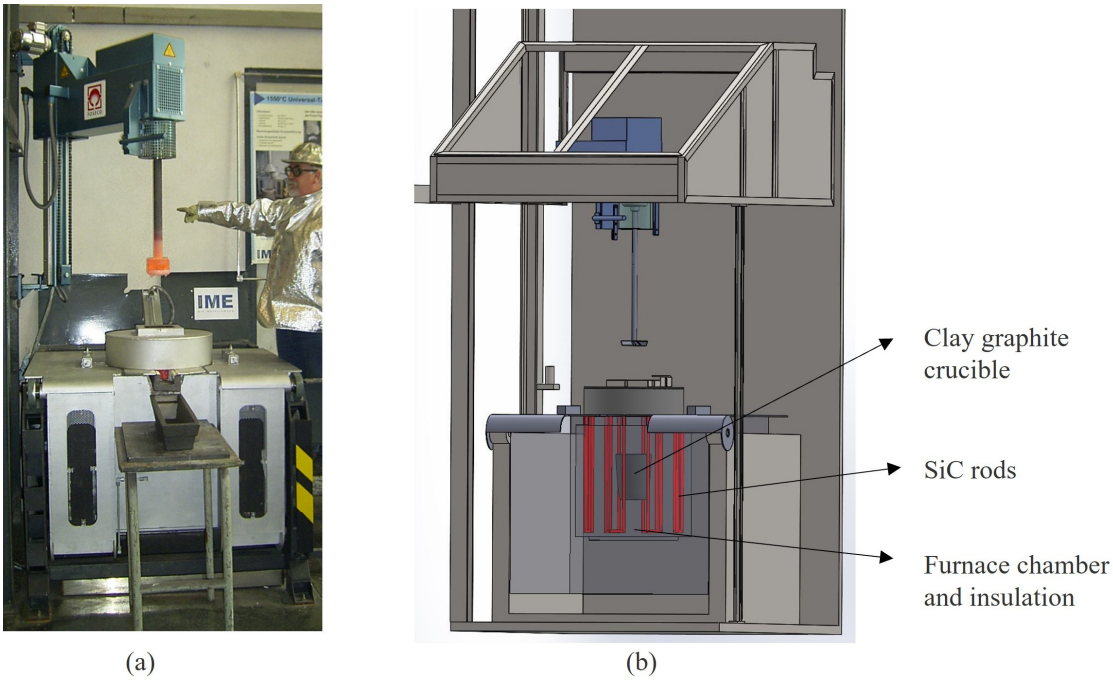

Figure 1. Electric furnace heating: (**a**) heating up the furnace during one experiment; (**b**) schematic design of the furnace.

2.1.2. Thermochemical Simulation

For thermochemical simulation, the phase diagram module from FactSage™ was used, with the databases FactPS and FTOxid. The predicted ternary diagram for the SiO_2-CaO-Al_2O_3, as shown in Figure 2, was calculated with a fixed amount of 8 wt.% of Li_2O and 10 wt.% MnO according to the defined composition of the artificial slag. The diagram was used to evaluate the liquidus temperature of the artificial slag. As highlighted by a red circle in Figure 2, the composition of the artificial slag used (EnAM) lies in a liquidus surface field between 1400 and 1450 °C; below 1500 °C, as desired. To evaluate the viscosity and the density of the artificial slag, the values in the diagrams shown in Figure 3 were calculated at the previously selected process temperature of 1500 °C. The viscosity model is based on the calculation of Gibbs Energy (FactSage™). As can be seen in (a), the expected viscosity of the artificial slag is between 0.15 and 0.2 Pa·s and the density lies in the range of 2.8 g/cm^3.

A solidification simulation was performed on the slag, based on the chemical composition presented in Table 2, using FactSage™ 8.2. Given that the simulation aims to predict the slag composition during the solidification process, the FToxid and FactPS databases were selected. The Scheil–Gulliver model was employed for this simulation, wherein the formed species are disregarded from the equilibrium and the overall mass balance. The solidification simulation was initiated with the slag in its fully liquid state, with a temperature step of 25 °C. Higher cooling rates could not be simulated in the model. The main mineral phases formed after solidification are represented in Table 3.

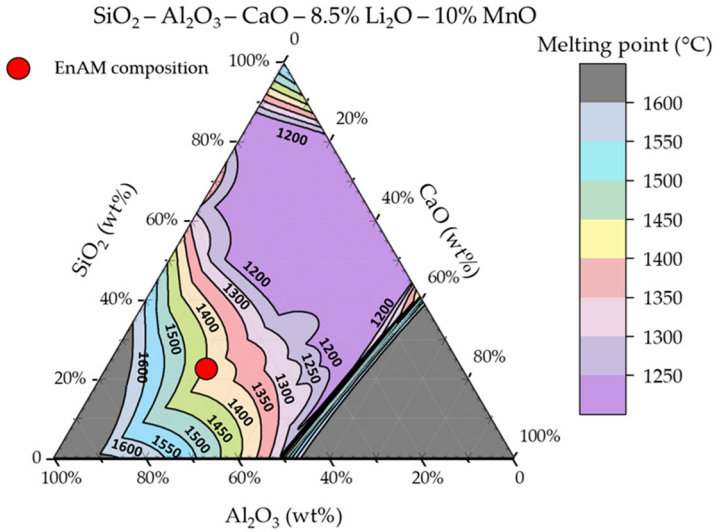

Figure 2. Diagram of predicted ternary SiO_2, CaO, and Al_2O_3 slag system with the projected liquidus surfaces according to FactSage™ [33].

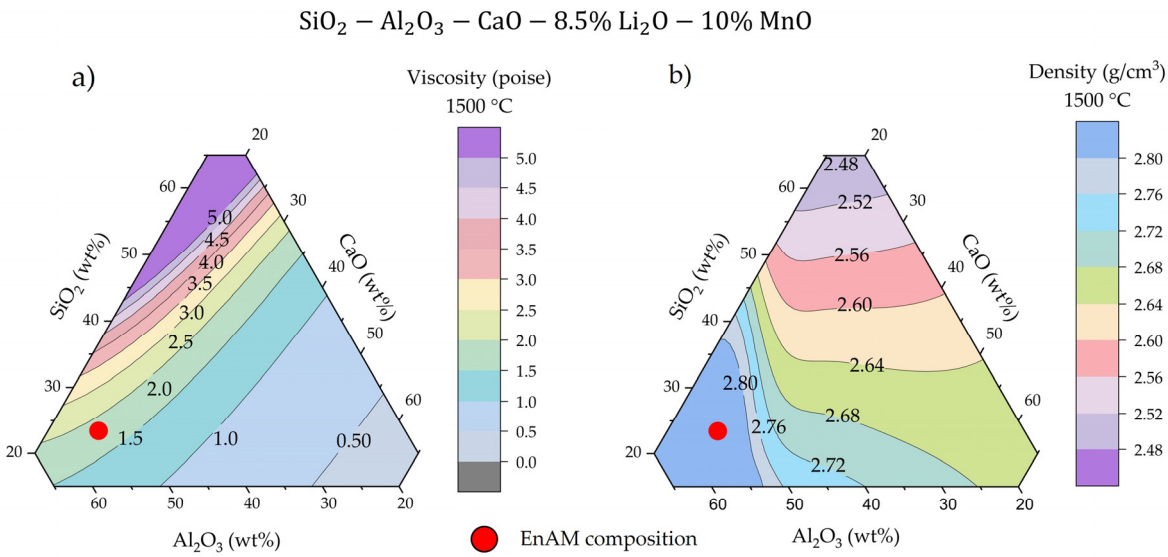

Figure 3. Diagram of predicted quasi-ternary SiO_2, CaO, and Al_2O_3 with the projected viscosity surfaces in poise (**a**) and density surfaces in g/cm³ (**b**) at 1500 °C according to FactSage™ [33].

Table 3. Predicted mineralogical composition of the slag after the solidification process according to FactSage™ 8.2.

Phase	$LiAl_5O_8$-Spinel	$Li_2Ca_2Si_2O_7$	$LiAlO_2$	Li_2SiO_3	Mn-Al Spinel	Gehlenite
wt.%	15.83	14.95	10.02	8.4	16.46	21.63

The primary lithium-containing phase formed based on the simulation is $LiAl_5O_8$-Spinel, while $Li_2Ca_2Si_2O_7$ is predicted as the second major mineral phase, followed by $LiAlO_2$ and Li_2SiO_3. Regarding the phases without lithium, Mn-Al spinel and gehlenite are the major minerals formed that do not contain lithium. Other minerals, each comprising less than 3 wt.%, are omitted from the representation. According to the simulation, the initial precipitated phase is a Li-Al spinel solid solution. Subsequently, $LiAl_5O_8$ precipitates, followed by the crystallisation of $LiAlO_2$-gamma. In addition to the precipitation of $LiAl_5O_8$, gehlenite is also formed. Mn-Al spinel is one of the last solid solutions to precipitate during the simulated solidification process. However, the existing thermochemical simulation

faces constraints due to the absence of a solid solution database. Consequently, the thermochemical outcomes may not accurately represent the actual experimental results. Based on prior studies on similar slag systems [8,20,21,27,28], it was observed that only $LiAlO_2$, as a Li-Al species, is identified in the experimental slag. It is worth noting that $LiAl_5O_8$, while theoretically plausible, is not found in the system based on these mentioned studies.

2.2. Methods for Characterisation

In this study, the characterization of lithium slag is conducted using X-ray micro-computed tomography (XCT), which provides 3D imaging of its inner structure. XCT offers valuable insights into the internal structure and grain morphology of the slag without destroying the sample. However, this method does not provide chemical or mineralogical phase composition, and therefore additional characterisation methods are necessary to complement the XCT result [34].

For this purpose, X-ray fluorescence (µXRF) analysis is utilized to provide element distribution information, while powder X-ray diffraction (XRD) identifies the mineralogical composition. The mineralogy of the slag phases is investigated on the flat surface of the middle part of the sample using µXRF and crushed samples are prepared for powder XRD analysis. These two analyses complement the morphological information provided by the XCT analysis, presenting a comprehensive view of the slag's properties. The integration of the above-mentioned methods facilitates a correlative characterization of the EnAM, offering a multi-dimensional understanding of the slag's characteristics.

The methodology of this study is illustrated in Figure 4. Initially, each slag sample is cut in half, vertically, down the middle, with a diamond cutter. This cut provides a flat surface on the centre of the slag body which is essential for µXRF which requires a horizontal surface. Subsequently, drill core samples with a 6 mm diameter are taken from the slag for XCT measurement to evaluate the grain structure and morphology in 3D. The drill cores are then crushed for XRD analysis to determine the phase composition present.

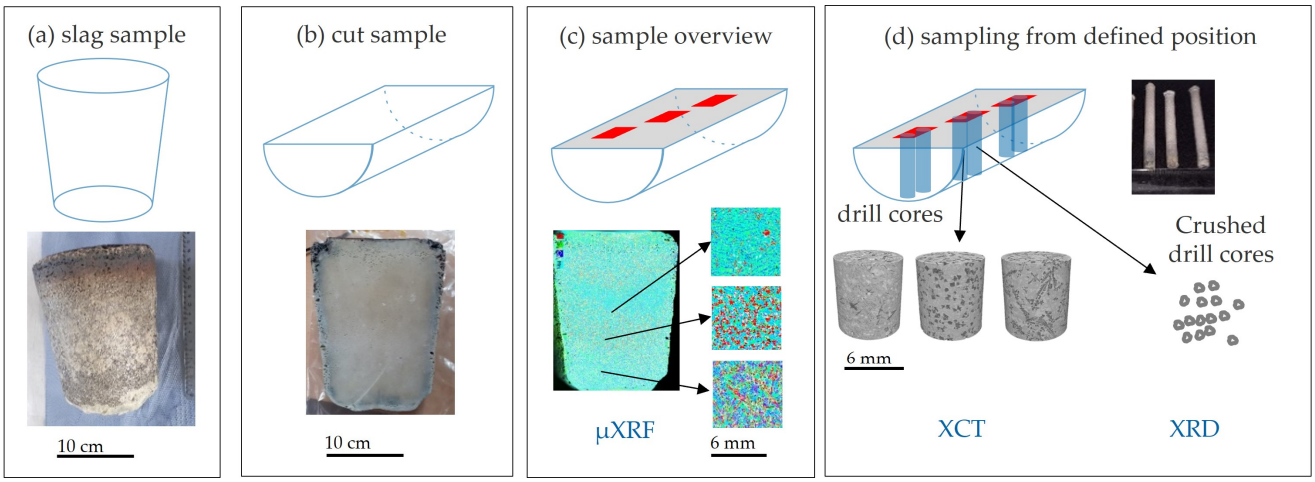

Figure 4. Overview of the work carried out in this study: (**a**) the whole slag sample; (**b**) after cutting the slag in half using a diamond cutter to obtain a flat surface in the middle of the slag; (**c**) micro X-ray fluorescence (µXRF) element mapping on the slag's flat surface to see heterogeneous structure along the slag; (**d**) drill core sampling of 6 mm diameter from different position where different structures can be identified for X-ray computer tomography (XCT) and X-ray diffraction (XRD) measurement.

2.2.1. Micro X-ray Fluorescence (µXRF)

An overview of the slag is important to ensure that the sampling for other measurement methods is representative and reflects the features of interest. To obtain an overview of the slag and its internal structure, 2D elemental mapping using M4 Tornado (Bruker Nano GmbH, Berlin, Germany) is carried out. The M4 Tornado uses micro X-ray fluorescence (µXRF) to give composition and visualise elemental distribution [35]. The µXRF

detector counts X-ray fluorescence energy that is emitted when the outer electron fills the inner shell of the excited atoms, and each atom has different energy spectra.

A challenge in lithium slag characterisation is the fact that lithium has a low atomic number. Not all elements in the periodic table can be quantified by XRF, especially elements lighter than sodium (Na), which do not emit radiation of accessible wavelength [36]. Provided that the phase of interest is lithium aluminate ($LiAlO_2$), the assumption that only Al is present in the element map is used. Despite the thermochemical simulation in Table 3 predicting another Li-Al species ($LiAl_5O_8$), it is expected that the experimental slag will incorporate $LiAlO_2$ as the main potential Li-Al species [28].

The first step is to acquire elemental maps of the whole slag surface and the vertical cutting plane, respectively, to quantify the inner structure of the slag and to determine whether it is homogenous or heterogeneous. In µXRF, the resolution is defined by the excited volume and the spacing between each measurement point. In this first overview measurement, a spacing of 150 µm is chosen. Additionally, this low-resolution measurement has the advantage of consuming less memory and having a shorter measurement duration. Based on the spectra and considering the feed composition, the elements present in the map are analysed. Following this initial analysis, a higher-resolution element map is acquired for the areas that have different structures to obtain a better insight into the EnAM structure and morphology, with 50 µm spot distance. The measurement parameters are listed in Table 4 below. This systematic approach, progressing from a broader overview to more focused mapping yields a comprehensive understanding of the slag elemental composition and distribution.

Table 4. Scan parameters for µXRF measurement.

Scan Parameter	Low Resolution	High Resolution
X-ray source	Rhodium (Rh)	
Acceleration voltage (W)	50	
Electrical power (W)	600	
spot size (µm)	20 µm	
measurement time/pixel (ms)	30	20
measurement point distance (µm)	150	50

2.2.2. X-ray Diffraction (XRD)

X-ray diffraction (XRD) measurement is used to determine and quantify the different phases in the slag. The measurement is conducted using Empyrean diffractometer (Malvern Panalytical, Almelo, The Netherlands). The drill cores are initially crushed using a steel mortar until <400 µm size fraction is achieved. Further milling of 2–2.5 mL of sample material with ethanol is performed using XRD-Mill McCrone (Retsch, Haan, Germany), with 12 min of milling time for each sample. Samples are prepared in a 27 mm diameter sample holder by applying the backloading technique to minimize preferred orientation issues. The measurement is carried out at 35 kV and 35 mA in the 2θ range of 5°–80° while keeping the irradiated area constant (12×15 mm^2) by means of an automated divergence slit. For the quantitative phase determination, Rietveld analysis using the open-source software package Profex/BGMN version 5.1.0 [37] is applied. This analytical method is suitable for analysing the presence of Li-bearing phases in the slag sample.

2.2.3. X-ray Computer Tomography (XCT)

After different morphologies are observed, drill core samples (6 mm in diameter) are taken from each different EnAM morphology to be measured with X-ray computer tomography (XCT). Images are obtained using ZEISS Xradia 510 Versa 3D X-ray microscope (Carl Zeiss, Oberkochen, Germany). Detailed information on XCT can be found in [38,39]. The scanning parameters are chosen based on the grey values of radiographs to provide a sufficient signal-to-noise ratio. The scan parameters are listed in Table 5.

Table 5. Scan parameters for XCT measurement.

Parameter	Value
Detector position (mm)	120
Source position (mm)	−16
Lens	0.4 X
Acceleration voltage (keV)	80
Electrical power (W)	7
Filter (Zeiss Standard)	LE5
Camera binning	2
Voxel size (µm)	8.07
Number of projections	1601
Scan angle (°)	360
Exposure time (s)	1.5
Scan time (hh:mm)	01:24

The reconstruction of the 2D radiographs is accomplished using a filtered back-projection algorithm implemented in Zeiss Reconstructor Scout-and-Scan version 16.1.13038. This includes an automatic centre shift and beam hardening correction with a factor of 0.05. The image data have to be further processed because of the presence of artefacts due to the XCT measurement, low contrast, and image noise.

The analysis of the 16-bit grey value image stack is conducted using ImageJ 1.53t (FIJI) and Dragonfly (v.2022.1., Objects Research Systems, Montréal, QC, Canada). These software solutions are used to process and visualise the reconstructed 3D volume. Image processing steps that are performed in this study include filtering and segmentation of the EnAMs using ImageJ (Figure 5). The filtering in ImageJ includes smoothing using a mean filter with a radius of 1.5 in all slices. This mean filter has a function to smooth the current image by replacing each pixel's value with the average grey value of its neighbouring pixels within the defined radius. Thresholding of the grey value was then carried out to segment the EnAMs using the value of 16,000 to 32,000. Afterwards, an erosion operation followed by dilation is performed to remove isolated pixels that surround the pores and the drill core. The histogram peaks in Figure 5a that occur before and after this segmented grey value correspond to the background (air) and the slag matrix, respectively. The slag matrix is shown as bright grey colours in Figure 5b that represent multi-phases in between the EnAMs.

The segmented EnAM binary images are further processed using Dragonfly software to obtain the volume and surface area features of the objects. This step is important for extracting their size and shape distribution. First, watershed transform was used to separate connected objects that occur due to the adjacent position of the EnAM grains. The binary images then were set to multi-ROI (region of interest) so that a single EnAM could be defined as an individual object. Information on each segmented object is obtained from component analysis in Dragonfly. The size (x_V) of each grain throughout this study is defined according to the volume equivalent sphere diameter (EQPS) and quantified in µm units.

$$x_V(\text{EQPS}) = \sqrt[3]{\frac{6}{\pi}V} \tag{1}$$

Feature volume (V) and surface area (As) information are used to calculate volume-equivalent sphere diameter and sphericity as the grain size and shape descriptor, respectively. Sphericity is calculated by comparing the calculated surface area to the equivalent sphere diameter and the actual surface area is directly obtained from the segmented image data [40]. The sphericity is calculated using the following equation:

$$\text{sphericity } \psi = \frac{\text{surface area of equivalent sphere}}{\text{surface area of grain}} = \frac{\pi {x_V}^2}{A_S} = \frac{\sqrt[3]{36\pi V^2}}{A_S} \tag{2}$$

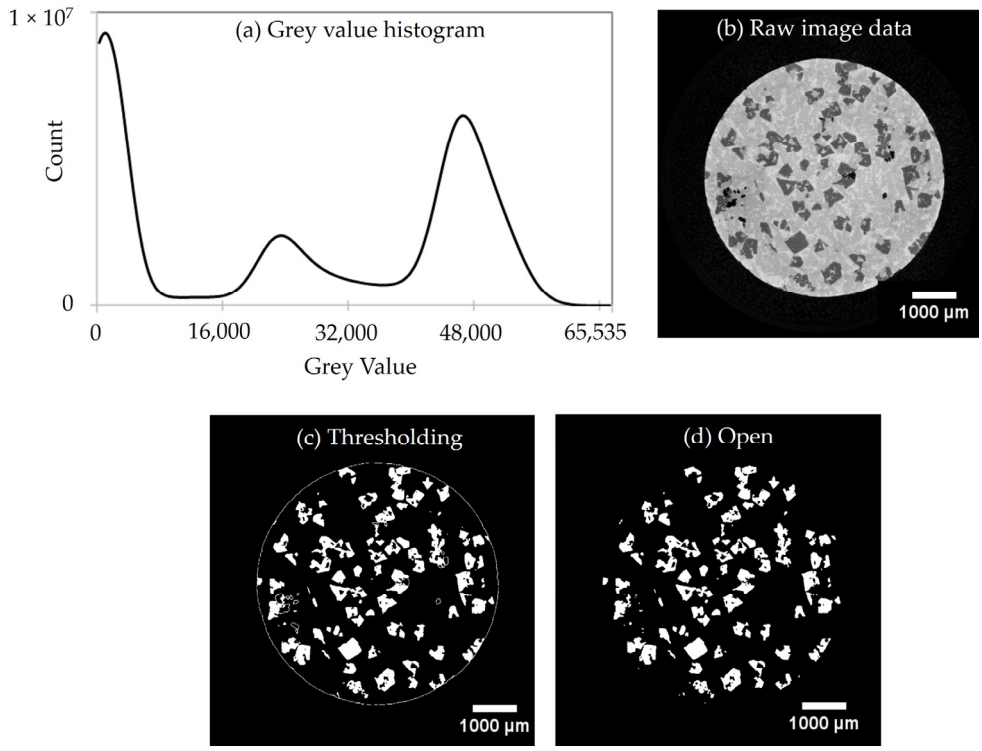

Figure 5. Image pre-processing in ImageJ: (**a**) grey value histogram of (**b**) raw image data after 2D reconstruction; (**c**) segmented objects after thresholding using 16,000–32,000; (**d**) morphological opening to remove isolated pixel objects.

3. Results

3.1. Slag Overview from µXRF, XRD and XCT

Referring to the characterisation method mentioned in Figure 4, the results of the µXRF, XRD and XCT analyses of Slag B (25 °C/h) are given in Figure 6. Image (a) on the left provides an initial overview scan of Slag B with 150 µm resolution. This offers a broad perspective of the slag's composition and structure. Meanwhile, images (b) and (c) show the element distribution at a higher resolution of 50 µm. The different colour maps represent different elements. The colour's intensity correlates to the energy counts in the detector, i.e., the abundance of an element. Images (a) and (c) highlight the overlay of the element distribution map. The red colour in the overlay map (c) represents the area in which only Al occurs. Since the EnAM is $LiAlO_2$, the occurrence of Al only (red spots) is considered to be the phase of interest, as mentioned in Section 2.2.

In Figure 6a, it can be observed that, in Slag B (25 °C/h), the upper and lower part of the crucible show the occurrence of dendritic EnAM, transitioning to granular crystals in the centre part with a gap in between, as shown in the upper part of Figure 6c. This gap indicates the region with a less visible occurrence of Al, as displayed in Figure 6b. The slag's structure varies along its height and can be grouped into three distinct structures that differ in their morphological properties.

The EnAM grains in the centre height of the slag (Slag B_G) have a more granular shape which is followed by dendritic-shaped grains on the lower part (Slag B_D). In contrast, the EnAM grains in Slag B_I show an irregular shape and size compared to those in Slag A_G and Slag B_G. In this context, irregular refers to grains lacking uniformity in size and shape. To investigate these morphological variations, three drill core samples are taken from these three different locations in Slag B. The results of the XCT measurement are given in Figure 6d,e. Additionally, Slag A (50 °C/h) shows a similar occurrence, but only with the granular and dendritic grain sequence, as depicted in Figure A1 under Appendix A.

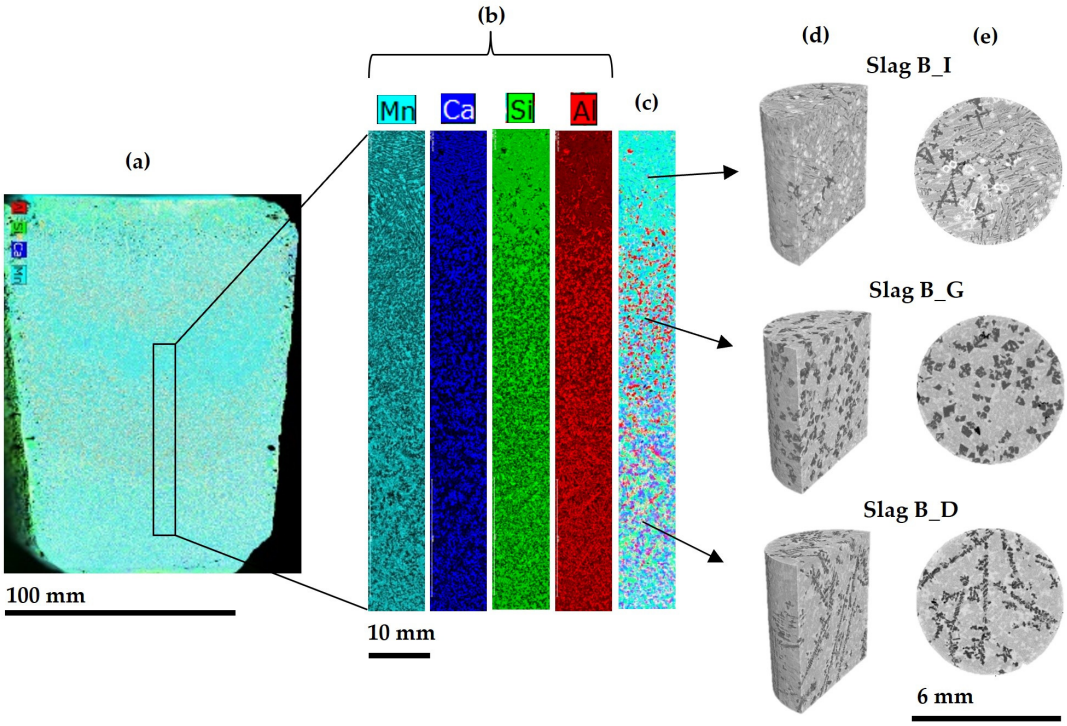

Figure 6. Element distribution in Slag B (25 °C/h) from µXRF (**a**–**c**) and XCT results (**d**,**e**) from drill core sample from selected position: (**a**) overlay of Al, Si, Ca, and Mn element map to obtain a chemical overview of the slag's horizontal flat surface with 150 µm resolution; (**b**) individual element map; (**c**) overlay of element map with 50 µm resolution in the area with different morphology transition; and (**d**) cut 3D volume of the drill cores and (**e**) the reconstructed horizontal cross section.

In the XCT measurement results, different greyscales represent different phases. At least three different greyscales are observed in the reconstructed XCT images. Based on the µXRF measurement and considering the density of the components, the dark greyscale is inferred to be the EnAM as $LiAlO_2$ has the lowest phase density compared to the other phases. This is confirmed since the results from the XCT images show that the dark grey phase corresponds to the Al distribution in the elemental map.

The XRD results, presented in Table 6, prove the presence of the different EnAM crystals. The corresponding XRD patterns are available for reference in the Appendix A, Figure A2. Samples for XRD were taken from defined positions that show different structures. $LiAlO_2$ appears to be the sole phase with a composition comprising Al, Li, and O. Considering the limitations of µXRF in detecting Li, the identification of areas containing only Al (without e.g., Si, cf. Table 6) represent the EnAM phase.

The gangue phases also vary between the different sampling positions. Sample G and D contain gehlenite and Mn-Al spinel as the major phase, with 35%–37% and 23%–25%, respectively, whereas sample I has more than 40% of gehlenite followed by 15% of glaucochroite. Nevertheless, Sample G has the highest mass percentage of EnAM and Li becomes highly concentrated in the EnAM phase, whereas, in the other areas of the slag body, some of the target element is dissipated in further phases.

The theoretical metallurgical yield suggests that up to 38% of Li from the feed is transformed to $LiAlO_2$. It should be noted that the quantification (and balancing) is based on an assumed 100% crystalline content as we did not find hints of any significant amorphous content. However, it cannot exclude the possibility that some elemental distribution is "hidden" in non-crystalline phases or exists as impurities in other phases. In addition, as some phases denote members of solid solutions (e.g., spinels and glaucochroite) with varying compositions, a full balancing is therefore difficult. Nevertheless, the results from XRD and the other methods are consistent.

Table 6. XRD results from Slag B (estimated standard deviation from Rietveld evaluation below 5%).

Mineral Phase in wt.%	Slag B_G	Slag B_D	Slag B_I
Lithium aluminate ($LiAlO_2$)	14.4	11.2	14.1
Eucryptite ($LiAlSiO_4$)	6.8	6.8	10.8
Lithium manganese silicate ($Li_2MnSiO4$)	9.6	7.7	9.1
Mn-Al spinel ($MnAl_2O_4$)	23.4	24.8	7.1
Gehlenite ($Ca_2Al_2SiO_7$)	35.0	37.3	43.5
Glaucochroite (Ca, Mn)$_2SiO_4$	10.1	11.4	15.1
Quartz (SiO_2)	<1	<1	<1
Total Li from $LiAlO_2$ in the sample (calculated) in wt.%	1.5	1.2	1.5
Total Li in the feed (calculated) in wt.%		3.9	
Total Li (feed) transformed into $LiAlO_2$ in %	38.4	29.9	37.6

In relation to the thermochemical simulation we performed, shown in Table 3, this XRD results and the simulation exhibit several species consistently and demonstrate the formation of specific phases during the simulated solidification process, including $LiAlO_2$, gehlenite, and Mn-Al spinel. The crystallisation of $LiAlO_2$ is indicated in the simulation, aligning with the XRD results and supporting the approach used to identify the EnAM. The formation of gehlenite and, finally, the generation of Mn-Al spinel in the simulation correlate with their presence in the XRD results, further validating the simulation's prediction. Li_2MnSiO_4 could not be predicted, as the database does not contain it. It is also noteworthy that $LiAlSiO_4$ was not predicted by the simulation, despite being identified in the XRD results. On the other hand, several Li-bearing phases, like $LiAl_5O_8$-Spinel, $Li_2Ca_2Si_2O_7$, and Li_2SiO_3, predicted in the simulation could not be detected in the XRD data. This may be due to the assumption used in the simulation that the lithium, silicate, aluminate, and carbonate are treated as an ideal solution, which is not realistic, as indicated by Sommerfeld et al. [8]. Additionally, the absence of solid solution database in the simulation strongly contributes to the discrepancy between the thermochemical simulation and the real experiment result [41]. The complexity of the real slag system is yet to be described more accurately by future simulations.

3.2. EnAM Morphology from XCT

Due to the high local yield of Li within the sample, the focus of this study will be the G areas with granular EnAM grain taken from the centre areas of both Slag A (50 °C/h) and Slag B (25 °C/h). These granular grains are of primary interest due to their favourable morphology for further mechanical processing. The visual comparison of Slag A_G and Slag B_G in Figure 7 gives an idea of different EnAMs formed through different cooling conditions.

Image (a) presents a 3D view of the drill cylinder of both slag from XCT, followed by image (b) providing a 2D cross-sectional view from the drill sample. Binary segmentation is depicted in image (c), where the white colour denotes the EnAM grains. Images (b) and (c) suggest that Slag B has more space between the single EnAM grains, facilitating liberation, whereas single grains of EnAM in Slag A seem to be connected to the neighbouring EnAM grains. This occurrence is also depicted in image (d), where distinct morphologies of both slags can be observed. This may be attributed to the different cooling rates of the slags. The slower cooling rate in Slag B seems to facilitate the growth of EnAM grains and allows the development of a more discrete grain structure. This characteristic may enhance and favour separation and potential liberation. In contrast, Slag A shows more closely interconnected EnAM grains. This proves the impact of cooling conditions on the properties of EnAM.

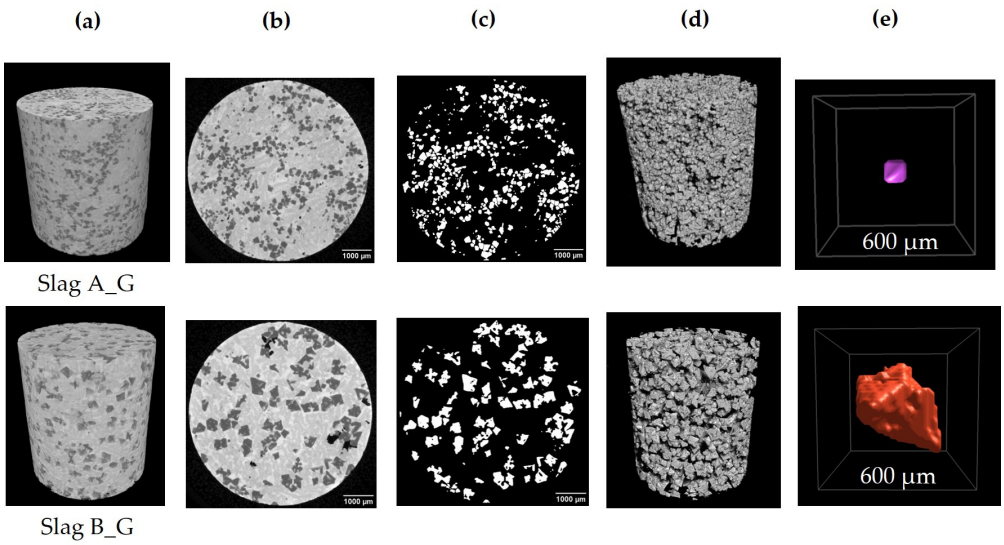

Figure 7. Visualisation of the EnAM morphology of sample G in Slag A (50 °C/h) and Slag B (25 °C/h): (**a**) 3D visualisation of the drill core sample; (**b**) 2D horizontal cross-sectional view; (**c**) segmented EnAM segmented as the object structure; (**d**) 3D morphology of the EnAM in drill core sample; (**e**) rendering of a single EnAM grain.

Figure 8 contains a probability density graph along with a continuous representation, through kernel density estimation (KDE), of the probability density of the two-dimensional EnAMs properties (size and shape) [42] from sample position G of the two slags. Here, a Gaussian kernel is used in the KDE using Python's scipy package [43]. The more detailed information on the processed XCT data is shown in Table A1. The grain size and sphericity used here are obtained from the calculated value using Equations (1) and (2), respectively, and are plotted as scatter plots on the left side of Figure 8. Slag A_G has a narrower and finer EnAM grain size distribution, from 33 µm to 510 µm, whereas the EnAMs in Slag B_G are distributed between 187 µm and 847 µm. The upper graph in Figure 8 represents the one-dimensional number-based probability density of the EnAM grain size distribution. Both size distributions have a median value of $x_{50,0}$ which is coarser than 100 µm (Table A1). The visual representation of a representative grain with a size close to x_{50} is shown in Figure 7e. Nevertheless, the $x_{90,0}$ of Slag B_G is more than two times coarser than Slag A_G, which are 583 µm and 227 µm, respectively.

Another important characteristic is the shape of the EnAM. The sphericity value in the vertical axis gives the idea that both slags have similar distribution widths, but with shifted distribution peaks. The EnAMs in Slag A_G have a sphericity which ranges from 0.35 to 0.95, while in Slag B_G this from 0.23 to 0.88. The one-dimensional probability density of the sphericity graph also shows that Slag A_G has more compact i.e., approximately spherical, EnAM grains, with a modal value of approximately 0.8. On the other hand, Slag B_G has a sphericity modal value of between 0.4 and 0.5. This sphericity value shows that Slag A_G, which has a faster cooling rate gradient, has a more isotropic shape compared to Slag B_G.

The different relationships between the grain size and sphericity are also shown by the KDE. In the case of Slag A_G, the narrow grain size distribution has a wider variety of shapes, containing both compact, almost spherical, grains as well as elongated grains. Conversely, for Slag B_G, larger grain sizes are characterized by reduced sphericity and by more dendritic particles, respectively. The volume-based probability density and a multidimensional scatter plot, where the radius of the circle plot corresponds to the grain volume, can also be seen in the Appendix A (Figure A3). The volume emphasizes the contribution of different grain sizes to the overall distribution.

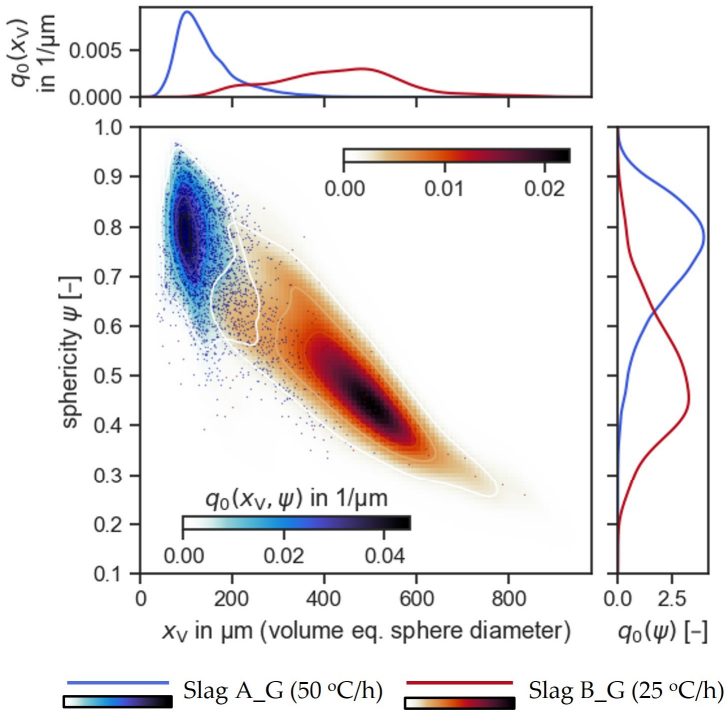

Figure 8. Number-based probability density distribution with continuous representation through kernel density estimation (KDE) from sampling area G of sample Slag A (50 °C/h) and Slag B (25 °C/h): volume-based where the radius of circle plots corresponds to grain volume.

4. Discussion

Crystal growth can be affected by microscopic interfacial dynamics and external macroscopic effects, such as the thermodynamic force. Depending on the equilibrium shape of the crystal system, dynamic equilibrium growth can lead to complex crystal growth, like dendritic growth [44]. In the case of $LiAlO_2$, the equilibrium shape of the crystal is compact, i.e., tetragonal for γ-$LiAlO_2$ [45]. The change in morphology over the height of the slag (Figure 6) suggests that the temperature gradients during cooling inside the slag body are neither homogenous nor isotropic. The observed morphological differences between the upper and lower parts, characterised by dendritic shape formations (D), and the centre region, identified by granular shape (G), in both slags investigated in this study reflect the variation of cooling velocities within the different part of the crucible. A similar occurrence of repeated granular–dendritic layers along the slag height was also observed in [46], where the crystallisation in dendritic areas indicates a steeper temperature gradient and a non-equilibrium condition. This study extends the understanding of crystallization dynamics, showing that the position within the crucible has a more prominent influence on the shape of the crystal grains compared to the cooling rates setting, as previously expected in [23].

These insights point to the need to combine these findings with an experimental measurement or a numerical simulation of the temperature field. This will provide the first quantitative hint about the temperature regime required for efficient EnAM production in this slag system. Moreover, enhancing the assumptions and databases employed in the thermochemical simulation will also be beneficial in narrowing the discrepancy between the thermochemical simulation result and the complexity of the real experimental result.

The slower cooling rate of Slag B (25 °C/h), compared to Slag A (50 °C/h), allows more time for the crystal to grow, resulting in a coarser grain size in the granular areas. This prolonged growth time may also be a factor which contributes to the lower sphericity in the Slag B sample, as the crystal may start to grow in a certain direction instead of equally growing in all directions. This is also supported by the grain size and sphericity plot in Figure 8, where the bigger the grain size tends to have the lower sphericity, which may be

connected to the overall thermodynamic properties of the different crystal plains in $LiAlO_2$. The shape development will need further research activities.

The gap between the granular grains in Slag B, identified as I, where irregular $LiAlO_2$ crystals are present, may occur due to the effect of density and viscosity differences during the first cooling and before the second holding time, at 1050 °C, of the melted feed materials which results in segregation, as seen in the μXRF results in Figure 6a–c. At this temperature, the lithium aluminate crystals initially nucleate, and therefore may have trapped the Ca and Si elements in this gap. Long molecule chains in silicate increase the melt viscosity and therefore crystallisation of these melts is slower. Amorphous phases are formed from these high-viscosity and fast-cooling liquids [47]. However, the XRD results in Table 6 shows that the gap, represented as Slag B_I, contains an adequate amount of $LiAlO_2$. This may indicate that the $LiAlO_2$ in this area is formed in nano to micron sizes that could not be resolved with either the μXRF or XCT measurements' resolution. To conduct a more detailed analysis of these hardly visible EnAM structures, it may be necessary to use another imaging technique, such as SEM-EDX analysis, which offers higher resolution for investigating the EnAM phases.

To improve the recyclability of lithium phases within the slag structure, the size and shape of the formed crystal play an important role. As mentioned before, that the recyclability of the lithium aluminate phase normally favours the coarser and granular shape, adjusting the production conditions to obtain the optimum slag structure may give better recovery on the potential processing process. However, this also depends on the breakage mechanism and the liberation of the phase of interest. This will require a more detailed understanding of how the crystal properties act on the behaviour of the EnAM materials during the mechanical process. If this is available, a relationship between mechanical processing parameters and slag crystallisation can be developed. Therefore, further analysis of the breakage and liberation behaviour of the different slag structures is necessary to finally evaluate the recyclability. Temperature distribution in this study was not quantified in detail as the temperature sensor only gives the temperature reading from one spot. The heat distribution and thermodynamics may need to be studied further as well to understand the structure build-up during slag crystallisation.

5. Conclusions

Synthetic model materials are used to synthesize lithium slag with different cooling rates of 50 and 25 °C/h. The valuable phase formed in the slag, or so-called engineered artificial mineral (EnAM), is lithium aluminate ($LiAlO_2$) as the phase of interest. In short, the main findings of this article can be summed up as follows:

- The μXRF analysis identifies variations in EnAM structures along the height of both slags.
- Three different qualities of the EnAM are defined based on the different morphology distributions of aluminium in μXRF to represent the occurrence of $LiAlO_2$, which are G for granular, D for dendritic, and I for the areas with irregular-shape EnAM.
- XCT images provide a quantified comparison between granular EnAM from the two slags with different cooling rates.
- The sample with the lower cooling rate (25 °C/h) has a coarser grain size in the granular areas, due to the lower cooling rate. The less spherical shape indicates that the crystal has a specific direction of growth.
- A faster cooling rate (50 °C/h) forms finer and more spherical EnAMs in the centre area, where the sampling for granular shape grains is taken for both slags.
- An interdisciplinary approach, e.g., metallurgy and mineral processing, is necessary to give a more detailed evaluation of the recycling process.

Despite challenges in analysing lithium, the correlation between the μXRF, XRD and XCT methods still provides valuable insights into the diverse EnAM morphologies formed. XCT imaging is particularly valuable for assessing the size and shape of the EnAMs, which is an important evaluation for the mechanical recycling process downstream. An optimi-

sation of the slag production process can also be carried out later by conducting further experiments with changes to the thermodynamics parameters, such as cooling rate, holding time, and holding temperature. An assessment of the breakage, liberation and recyclability of the slag has to be the focus of further studies. Additionally, a comprehensive investigation into the crystallisation process and nucleation of lithium aluminate crystal should supplement the mineral processing. Deeper insights into heat transfer and thermochemical simulation during slag production will enhance the understanding of EnAM formation and enhance the recyclability of metallurgical slag systems.

Author Contributions: Conceptualization, C.R., E.L. and T.L.; methodology, C.R., J.W. and H.I.L.; formal analysis, C.R., J.W., H.I.L., E.L., D.E. and R.M.; investigation, C.R., J.W. and H.I.L.; writing—original draft preparation, C.R. and J.W.; writing—review and editing, E.L., T.L., D.E., R.M., B.F. and U.A.P.; visualisation, C.R. and J.W.; supervision, E.L., T.L., H.I.L., B.F. and U.A.P.; funding acquisition, B.F. and U.A.P. All authors have read and agreed to the published version of the manuscript.

Funding: This research was funded by the Deutsche Forschungsgemeinschaft (DFG, German Research Foundation) in the priority program 2315 "Engineered artificial minerals (EnAM)—A geometallurgical tool to recycle critical elements from waste streams" with grant number 470552553.

Data Availability Statement: The data presented in this study are available upon request from the corresponding author.

Acknowledgments: The authors acknowledge the financial support of the DFG, which made this project possible; and Helmholtz Institute Freiberg for providing the M4 Tornado µXRF equipment and Roland Wuerkert for cutting the sample.

Conflicts of Interest: The authors declare no conflicts of interest. The funders had no role in the design of the study; in the collection, analyses, or interpretation of data; in the writing of the manuscript; or in the decision to publish the results.

Appendix A

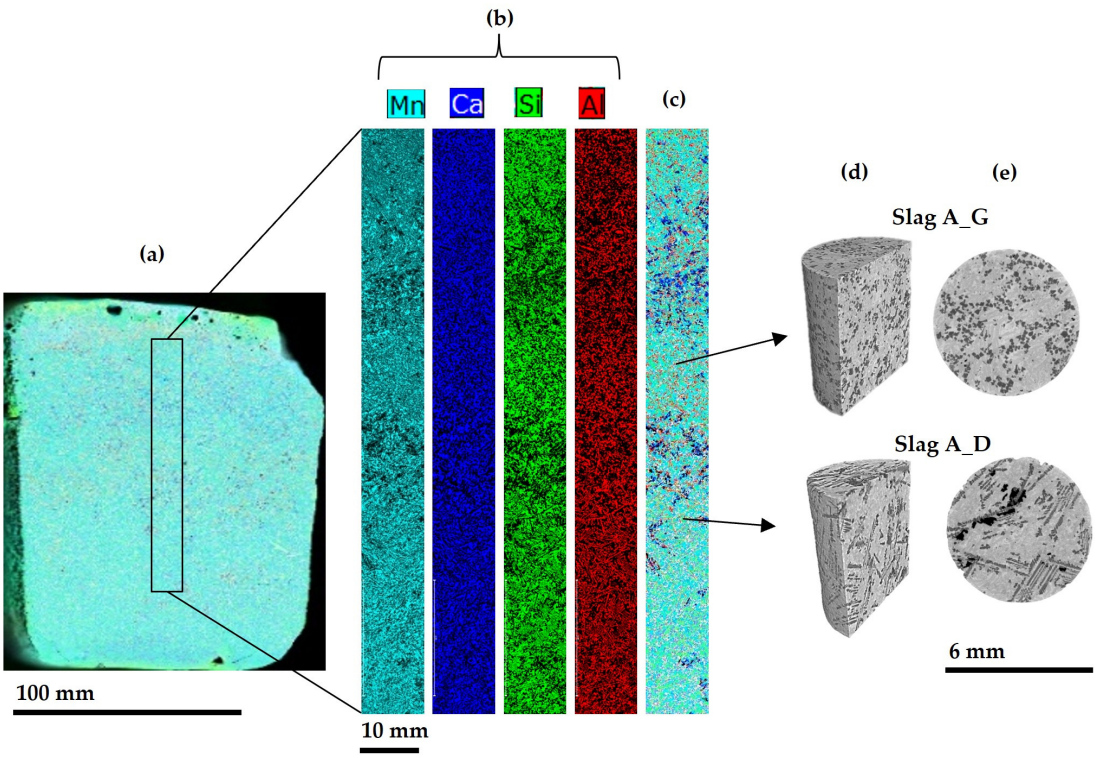

Figure A1. Element distribution in Slag A (50 °C/h) from µXRF (**a**–**c**) and XCT results (**d**,**e**) from drill core sample from selected position: (**a**) Overlay of Al, Si, Ca, and Mn element map to obtain a chemical

overview of the slag horizontal flat surface with 150 µm resolution; (**b**) individual element map and; (**c**) overlay of element map with 50 µm resolution in the area with different morphology transition; (**d**) cut 3D volume of the drill cores and (**e**) the reconstructed horizontal cross section.

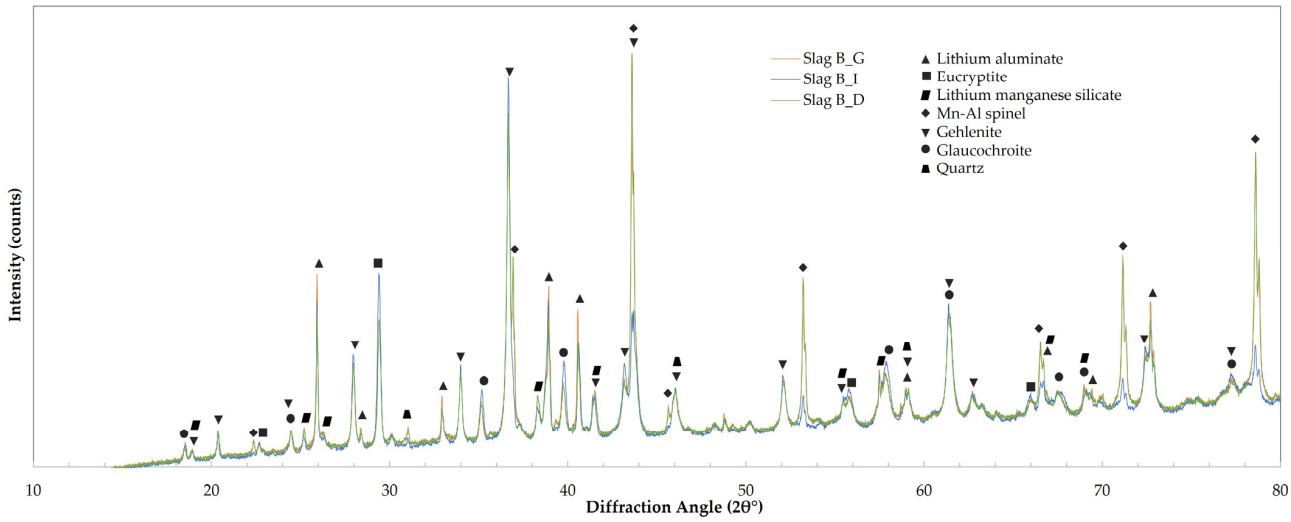

Figure A2. XRD pattern of the Slag B (25 °C/h).

Table A1. EnAM analysis from XCT results.

XCT Analysis	Slag A_G	Slag B_G
analysed drill core (µm^3)	1.9×10^{11}	1.9×10^{11}
segmented EnAM (µm^3)	4.1×10^{10}	3.6×10^{10}
$x_{10,0}$ (µm)	80	224
$x_{50,0}$ (µm)	125	433
$x_{90,0}$ (µm)	227	583

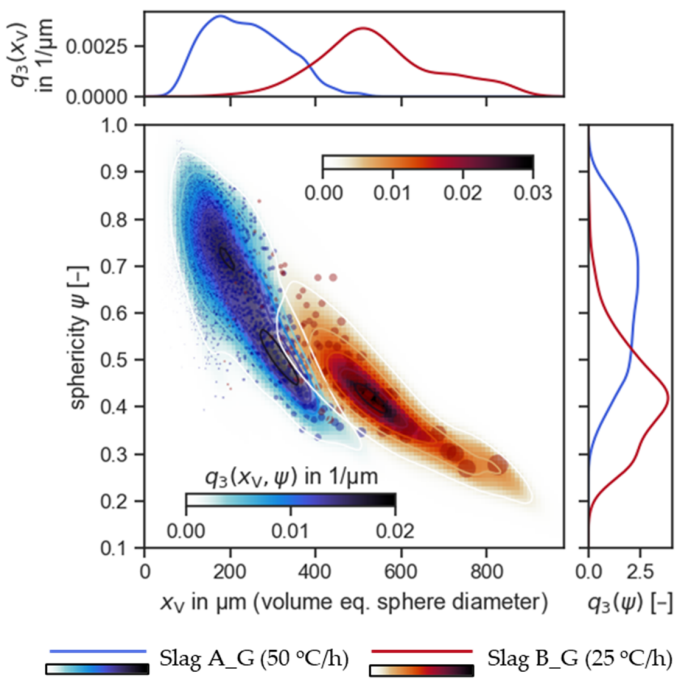

Figure A3. Volume-based probability density distribution with continuous representation through kernel density estimation (KDE) from sampling area G of sample Slag A (50 °C/h) and Slag B (25 °C/h). The radius of the circle plots corresponds to grain volume.

References

1. International Energy Agency (IEA). *Global Electric Vehicle Outlook 2022*; IEA: Paris, France, 2022.
2. Shine, I. The World Needs 2 Billion Electric Vehicles to Get to Net Zero. But Is There Enough Lithium to Make All the Batteries? Available online: https://www.weforum.org/agenda/2022/07/electric-vehicles-world-enough-lithium-resources/ (accessed on 20 July 2022).
3. Castelvecchi, D. Electric Cars and Batteries: How Will the World Produce Enough? *Nature* **2021**, *596*, 336–339. [CrossRef]
4. Fleischmann, J.; Schaufuss, P.; Linder, M.; Hanicke, M.; Horetsky, E.; Ibrahim, D.; Jautelat, S.; Torscht, L.; De Van Rijt, A. Battery 2030: Resilient, Sustainable, and Circular. Battery Demand Is Growing—And So Is the Need for Better Solutions along the Value Chain. Available online: https://www.mckinsey.com/industries/automotive-and-assembly/our-insights/battery-2030-resilient-sustainable-and-circular (accessed on 16 January 2023).
5. Baum, Z.J.; Bird, R.E.; Yu, X.; Ma, J. Lithium-Ion Battery Recycling—Overview of Techniques and Trends. *Acs Energy Lett.* **2022**, *7*, 712–719. [CrossRef]
6. Lemougna, P.N.; Yliniemi, J.; Ismailov, A.; Levanen, E.; Tanskanen, P.; Kinnunen, P.; Roning, J.; Illikainen, M. Recycling Lithium Mine Tailings in the Production of Low Temperature (700–900 °C) Ceramics: Effect of Ladle Slag and Sodium Compounds on the Processing and Final Properties. *Constr. Build. Mater.* **2019**, *221*, 332–344. [CrossRef]
7. Zhou, M.; Li, B.; Li, J.; Xu, Z. Pyrometallurgical Technology in the Recycling of A Spent Lithium Ion Battery: Evolution and the Challenge. *ACS EST Eng.* **2021**, *1*, 1369–1382. [CrossRef]
8. Sommerfeld, M.; Vonderstein, C.; Dertmann, C.; Klimko, J.; Oráč, D.; Miškufová, A.; Havlík, T.; Friedrich, B. A Combined Pyro- And Hydrometallurgical Approach to Recycle Pyrolyzed Lithium-Ion Battery Black Mass Part 1: Production of Lithium Concentrates in An Electric Arc Furnace. *Metals* **2020**, *10*, 1069. [CrossRef]
9. Werner, D.; Peuker, U.A.; Mütze, T. Recycling Chain For Spent Lithium-Ion Batteries. *Metals* **2020**, *10*, 316. [CrossRef]
10. Wuschke, L.; Jäckel, H.-G.; Leißner, T.; Peuker, U.A. Crushing Of Large Li-Ion Battery Cells. *Waste Manag.* **2019**, *85*, 317–326. [CrossRef]
11. Reinhart, L.; Vrucak, D.; Woeste, R.; Lucas, H.; Rombach, E.; Friedrich, B.; Letmathe, P. Pyrometallurgical Recycling of Different Lithium-Ion Battery Cell Systems: Economic And Technical Analysis. *J. Clean. Prod.* **2023**, *416*, 137834. [CrossRef]
12. Chen, M.; Ma, X.; Chen, B.; Arsenault, R.; Karlson, P.; Simon, N.; Wang, Y. Recycling End-Of-Life Electric Vehicle Lithium-Ion Batteries. *Joule* **2019**, *3*, 2622–2646. [CrossRef]
13. Windisch-Kern, S.; Holzer, A.; Ponak, C.; Raupenstrauch, H. Pyrometallurgical Lithium-Ion-Battery Recycling: Approach to Limiting Lithium Slagging With the Indured Reactor Concept. *Processes* **2021**, *9*, 84. [CrossRef]
14. Holzer, A.; Windisch-Kern, S.; Ponak, C.; Raupenstrauch, H. A Novel Pyrometallurgical Recycling Process for Lithium-Ion Batteries And Its Application to the Recycling Of Lco And Lfp. *Metals* **2021**, *11*, 149. [CrossRef]
15. Bae, H.; Kim, Y. Technologies of Lithium Recycling From Waste Lithium Ion Batteries: A Review. *Mater. Adv.* **2021**, *2*, 3234–3250. [CrossRef]
16. Werner, D.M.; Mütze, T.; Kaas, A.; Peuker, U.A. Mechanical And Physical Processes of Battery Recycling. In *Nano Technology for Battery Recycling, Remanufacturing, And Reusing*; Elsevier: Amsterdam, The Netherlands, 2022; pp. 455–486.
17. Wilke, C.; Werner, D.M.; Kaas, A.; Peuker, U.A. Influence of the Crusher Settings And A Thermal Pre-Treatment on the Properties of the Fine Fraction (Black Mass) From Mechanical Lithium-Ion Battery Recycling. *Batteries* **2023**, *9*, 514. [CrossRef]
18. Dang, H.; Chang, Z.; Zhou, H.; Ma, S.; Li, M.; Xiang, J. Extraction of Lithium From the Simulated Pyrometallurgical Slag of Spent Lithium-Ion Batteries By Binary Eutectic Molten Carbonates. *Int. J. Miner. Met. Mater.* **2022**, *29*, 1715–1721. [CrossRef]
19. Shen, H.; Forssberg, E. An Overview of Recovery of Metals From Slags. *Waste Manag.* **2003**, *23*, 933–949. [CrossRef]
20. Schirmer, T.; Qiu, H.; Li, H.; Goldmann, D.; Fischlschweiger, M. Li-Distribution in Compounds of the Li_2o-Mgo-Al_2o_3-Sio_2-Cao System—A First Survey. *Metals* **2020**, *10*, 1633. [CrossRef]
21. Elwert, T.; Goldmann, D.; Strauss, K.; Schirmer, T. Phase Composition of High Lithium Slags from the Recycling of Lithium Ion Batteries. *World Metall. Erzmetall* **2012**, *65*, 163–171.
22. Bale, C.W.; Chartrand, P.; Degterov, S.A.; Eriksson, G.; Hack, K.; Ben Mahfoud, R.; Melançon, J.; Pelton, A.D.; Petersen, S. Factsage Thermochemical Software and Databases. *Calphad* **2002**, *26*, 189–228. [CrossRef]
23. Buchmann, M.; Borowski, N.; Leißner, T.; Heinig, T.; Reuter, M.A.; Friedrich, B.; Peuker, U.A. Evaluation of Recyclability of A Weee Slag By Means Of Integrative X-Ray Computer Tomography And Sem-Based Image Analysis. *Minerals* **2020**, *10*, 309. [CrossRef]
24. Hewlett, P.C.; Liška, M. (Eds.) *Lea's Chemistry of Cement And Concrete*; Butterworth-Heinemann: Oxford, UK; Cambridge, UK, 2019.
25. Reyes, F.; Lin, Q.; Cilliers, J.J.; Neethling, S.J. Quantifying Mineral Liberation by Particle Grade And Surface Exposure Using X-Ray Microct. *Miner. Eng.* **2018**, *125*, 75–82. [CrossRef]
26. Leißner, T.; Mütze, T.; Bachmann, K.; Rode, S.; Gutzmer, J.; Peuker, U.A. Evaluation of Mineral Processing by Assessment of Liberation And Upgrading. *Miner. Eng.* **2013**, *53*, 171–173. [CrossRef]
27. Wittkowski, A.; Schirmer, T.; Qiu, H.; Goldmann, D.; Fittschen, U.E.A. Speciation of Manganese in A Synthetic Recycling Slag Relevant for Lithium Recycling from Lithium-Ion Batteries. *Metals* **2021**, *11*, 188. [CrossRef]
28. Schirmer, T.; Wahl, M.; Bock, W.; Kopnarski, M. Determination of the Li Distribution in Synthetic Recycling Slag with Sims. *Metals* **2021**, *11*, 825. [CrossRef]

29. Shin, J.; Jeong, J.-M.; Lee, J.B.; Heo, N.S.; Kwon, H.; Kim, Y.H.; Ryu, T. Recovery of Lithium from Lialo2 in Waste Box Sagger Through Sulfation to Produce Li2so4 And Sequential Wet Conversion to Li3po4, Licl And Li2co3. *Hydrometallurgy* **2023**, *215*, 105988. [CrossRef]
30. Fandrich, R.G.; Bearman, R.A.; Boland, J.; Lim, W. Mineral Liberation by Particle Bed Breakage. *Miner. Eng.* **1997**, *10*, 175–187. [CrossRef]
31. King, R.P.; Schneider, C.L. Mineral Liberation And the Batch Comminution Equation. *Miner. Eng.* **1998**, *11*, 1143–1160. [CrossRef]
32. Lennartsson, A.; Engström, F.; Samuelsson, C.; Björkman, B.; Pettersson, J. Large-Scale Weee Recycling Integrated in An Ore-Based Cu-Extraction System. *J. Sustain. Metall.* **2018**, *4*, 222–232. [CrossRef]
33. Bale, C.W.; Bélisle, E.; Chartrand, P.; Decterov, S.A.; Eriksson, G.; Gheribi, A.E.; Hack, K.; Jung, I.-H.; Kang, Y.-B.; Melançon, J.; et al. Factsage Thermochemical Software and Databases, 2010–2016. *Calphad* **2016**, *54*, 35–53. [CrossRef]
34. Fittschen, U.E.; Möckel, R.; Schreiner, M.; Klinger, M.; Radtke, M.; Meyer, B.; Guhl, S.; Renno, A.; Godinho, J.; Gloaguen, R.; et al. Bundling Analytical Capacities to Understand Phase Formation in Recycling of Functional Materials. *Msf* **2019**, *959*, 183–190. [CrossRef]
35. Kaskes, P.; Déhais, T.; De Graaff, S.J.; Goderis, S.; Claeys, P. Micro–X-ray Fluorescence (µxrf) Analysis of Proximal Impactites: High-Resolution Element Mapping, Digital Image Analysis, and Quantifications. In *Large Meteorite Impacts And Planetary Evolution Vi*; Reimold, W.U., Koeberl, C., Eds.; Geological Society of America: Boulder, CO, USA, 2021; pp. 171–206.
36. Beckhoff, B.; Kanngießer, B.; Langhoff, N.; Wedell, R.; Wolff, H. (Eds.) *Handbook of Practical X-ray Fluorescence Analysis*; Springer: Berlin/Heidelberg, Germany, 2006.
37. Doebelin, N.; Kleeberg, R. Profex: A Graphical User Interface for the Rietveld Refinement Program Bgmn. *J. Appl. Crystallogr.* **2015**, *48*, 1573–1580. [CrossRef] [PubMed]
38. Withers, P.J.; Bouman, C.; Carmignato, S.; Cnudde, V.; Grimaldi, D.; Hagen, C.K.; Maire, E.; Manley, M.; Du Plessis, A.; Stock, S.R. X-Ray Computed Tomography. *Nat. Rev. Methods Primers* **2021**, *1*, 18. [CrossRef]
39. Hanna, R.D.; Ketcham, R.A. X-Ray Computed Tomography of Planetary Materials: A Primer And Review of Recent Studies. *Geochemistry* **2017**, *77*, 547–572. [CrossRef]
40. Wadell, H. Volume, Shape, And Roundness of Rock Particles. *J. Geol.* **1932**, *40*, 443–451. [CrossRef]
41. Li, H.; Ranneberg, M.; Fischlschweiger, M. High-Temperature Phase Behavior of Li2o-Mno with A Focus on the Liquid-To-Solid Transition. *JOM* **2023**, *75*, 5796–5807. [CrossRef]
42. Buchwald, T.; Schach, E.; Peuker, U.A. A Framework for the Description of Multidimensional Particle Separation Processes. *Powder Technol.* **2024**, *433*, 119165. [CrossRef]
43. Virtanen, P.; Gommers, R.; Oliphant, T.E.; Haberland, M.; Reddy, T.; Cournapeau, D.; Burovski, E.; Peterson, P.; Weckesser, W.; Bright, J.; et al. Scipy 1.0: Fundamental Algorithms for Scientific Computing in Python. *Nat. Methods* **2020**, *17*, 261–272. [CrossRef] [PubMed]
44. Ben-Jacob, E.; Garik, P. The Formation of Patterns in Non-Equilibrium Growth. *Nature* **1990**, *343*, 523–530. [CrossRef]
45. Heo, S.J.; Batra, R.; Ramprasad, R.; Singh, P. Crystal Morphology And Phase Transformation of Lialo 2: Combined Experimental And First-Principles Studies. *J. Phys. Chem. C* **2018**, *122*, 28797–28804. [CrossRef]
46. Bhagurkar, A.G.; Qin, R. The Microstructure Formation in Slag Solidification at Continuous Casting Mold. *Metals* **2022**, *12*, 617. [CrossRef]
47. Tossavainen, M.; Engstrom, F.; Yang, Q.; Menad, N.; Lidstrom Larsson, M.; Bjorkman, B. Characteristics of Steel Slag under Different Cooling Conditions. *Waste Manag.* **2007**, *27*, 1335–1344. [CrossRef]

Disclaimer/Publisher's Note: The statements, opinions and data contained in all publications are solely those of the individual author(s) and contributor(s) and not of MDPI and/or the editor(s). MDPI and/or the editor(s) disclaim responsibility for any injury to people or property resulting from any ideas, methods, instructions or products referred to in the content.